Dispersionless gaps and cavity modes in photonic crystals containing hyperbolic metamaterials

Chun-hua Xue,[1,2] Yaqiong Ding,[1,3] Hai-tao Jiang,[1,*] Yunhui Li,[1] Zhan-shan Wang,[1] Ye-wen Zhang,[1] and Hong Chen[1]

[1]*Tongji University, Shanghai 200092, China*

[2]*School of Computer Science & Communication Engineering, Guangxi University of Science and Technology, Liuzhou, Guangxi 545006, China*

[3]*Science College, University of Shanghai for Science and Technology, Shanghai 200093, China*

(Received 4 November 2015; revised manuscript received 1 March 2016; published 22 March 2016)

We theoretically study dispersionless gaps and cavity modes in one-dimensional photonic crystals composed of hyperbolic metamaterials and dielectric. Bragg gaps in conventional all-dielectric photonic crystals are always dispersive because propagating phases in two kinds of dielectrics decrease with incident angle. Here, based on phase variation compensation between a hyperbolic metamaterial layer and an isotropic dielectric layer, the dispersion of the gap can be offset and thus a dispersionless gap can be realized. Moreover, the dispersionless property of such gap has a wide parameter space. The dispersionless gap can be used to realize a dispersionless cavity mode. The dispersionless gaps and cavity modes will possess significant applications for all-angle reflectors, high-Q filters excited with finite-sized sources, and nonlinear wave mixing processes.

DOI: 10.1103/PhysRevB.93.125310

I. INTRODUCTION

Photonic crystals (PCs) are artificial materials with a periodic spatial modulation in the dielectric constant which can suppress the propagation of light by opening a photonic band gap within a given range of frequencies [1,2]. They exhibit many novel phenomena and propel enormous applications by engineering a photonic band gap. In view of applications, an omnidirectional gap which can reflect electromagnetic waves in all directions is highly desirable [3,4]. In one-dimensional (1D) all-dielectric PCs, omnidirectional gaps are realized from relatively wide Bragg gaps whose edges change with the incident angles. However, if one can realize a gap whose edges are independent of the incident angles, one can further obtain a dispersionless (omnidirectional) gap with a fixed bandwidth. Typical examples include zero average index (zero-$\bar{n}$) gap [5–8] and zero effective phase (zero-ϕ_{eff}) gap [9,10]. The dispersionless properties of zero-$\bar{n}$ gap originate from the phase cancellation of propagating waves between positive- and negative-index materials [11]. On the other hand, the dispersionless properties of zero-ϕ_{eff} gap originate from the compensation of the exponentially increasing and the exponentially decreasing waves in a one-dimensional photonic crystal (1DPC) containing two kinds of single-negative materials. Zero-$\bar{n}$ gap [12] and zero-ϕ_{eff} gap [13] were firstly observed in the microwave region. However, in the near-infrared or the visible region, negative-index materials or negative-permeability materials are hard to implement, which limit the experimental realizations of dispersionless gaps. Only recently, people have used a two-dimensional PC to mimic a negative-index material and experimentally observe the zero-$\bar{n}$ gap at near-infrared frequencies [14,15].

In this paper we explore the possibilities of realizing dispersionless gaps in a simple one-dimensional structure, i.e., a 1DPC composed of layered hyperbolic metamaterials (HMMs) and dielectrics. HMMs are highly anisotropic media with hyperbolic dispersion [16]. Such metamaterials are quite different from conventional (uniaxial) crystals in which one of the principal components of their permittivity (permeability) tensors is opposite in sign to the other two principal components. In the near-infrared or visible region, a 1D metal-dielectric stack with subwavelength unit cell can mimic HMMs [17–19], which provides a convenient method for the experimental implementation of HMMs. HMMs support propagating modes with very large wave vectors (also called high-k waves), which brings about a rich variety of new physics and novel applications, including negative refraction, and hyperlens as well as spontaneous and thermal emission engineering (see [20,21] and references therein). More interesting, owing to the high-k waves in HMM, a 1D stack composed of a deeply subwavelength HMM layer and dielectric layer, so-called photonic hypercrystals [22,23], can offer an unprecedented way to control the light propagation and thus activate novel physical phenomena such as surface wave engineering and the Veselago lens. Nevertheless, most studies of HMMs have focused on the high-k waves so far [24,25]. In fact, the HMMs not only support high-k waves, but also possess anomalous wave-vector dispersion by contrast with isotropic dielectric. Here we investigate the dispersionless gaps in 1DPCs containing HMMs. Different from the 1D stack in Ref. [22], the size of the HMM layer and dielectric layer in our design is in the scale of the wavelength although the metal-dielectric substructure used to mimic the HMM is very subwavelength (i.e., the size of the unit cell in the substructure is about one-thirtieth of the wavelength). Our studies reveal the phase variation compensation effect between a HMM layer and a dielectric layer which comes from the anomalous wave-vector dispersion of HMMs. It is this effect that makes the photonic gap invariant with incident directions. Moreover, this effect exists in a wide parameter space and can be used to design dispersionless cavity modes.

This paper is organized as follows. In Sec. II, we start from the lossless case to study the phase variation compensation effect between a HMM layer and a dielectric layer and derive the conditions of a dispersionless gap. Then based on the analytical conditions, we use a 1D metal-dielectric stack to mimic a HMM and realize the dispersionless gaps in the

*Corresponding author: jiang-haitao@tongji.edu.cn

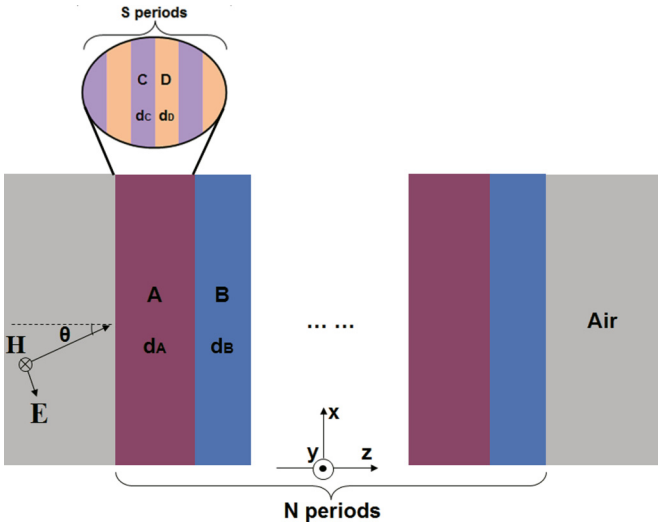

FIG. 1. The scheme of a 1DPC composed of a HMM layer and an isotropic dielectric layer, which is denoted by $(AB)_N$. HMM layer A is mimicked by a metal-dielectric layered substructure $(CD)_S$ with a subwavelength unit cell. $d_A = S(d_C + d_D)$. The background is air.

1DPCs containing the effective HMMs. Next we discuss the influence of loss on the design of dispersionless gaps. Later dispersionless gaps are found to survive in a wide parameter space. In Sec. III, we study an important application of the dispersionless gaps, i.e., dispersionless cavity modes. Finally, the Conclusion is given in Sec. IV.

II. PHASE VARIATION COMPENSATION EFFECTS AND DISPERSIONLESS GAPS

A. The lossless case

We consider a 1DPC composed of a HMM layer and an isotropic material layer, which is denoted by $(AB)_N$. As is shown in Fig. 1, medium A is a HMM with anisotropic permittivity tensor diag$(\varepsilon_{Ax},\varepsilon_{Ax},\varepsilon_{Az})$ and medium B is an isotropic dielectric with permittivity ε_B. In this part we consider the lossless case and thus the values of permittivity are real numbers. d_A and d_B are the thicknesses of two inclusion layers, respectively, and $d = d_A + d_B$ is the length of the unit cell. Moreover, medium A and B are supposed as nonmagnetic, i.e., $\mu_A = \mu_B = 1$. N is the number of periods. The background is air.

We consider that electromagnetic waves with transverse-magnetic (TM) polarization launch into the structure in the x-z plane with an incident angle θ, as is shown in Fig. 1. The magnetic field is in the y direction. Here we take $k_y = 0$ without loss of generality as due to the planar geometry we can always find a coordinate system where $k_y = 0$. Normally, both ordinary wave and extraordinary wave will occur in a HMM. However, in Fig. 1, the optical axis of HMM is along the z direction and the magnetic field of a TM polarized wave is perpendicular to the optical axis. In this case, as is demonstrated in the Appendix, only an extraordinary wave is excited in the HMM layer and the isofrequency contour of medium A is given by

$$\frac{k_x^2}{\varepsilon_{Az}} + \frac{k_{Az}^2}{\varepsilon_{Ax}} = k_0^2, \tag{1}$$

where $k_x = k_0 \sin\theta$ is the x component of the wave vector, k_{Az} is the z component of the wave vector in medium A, and $k_0 = \omega/c$ is the wave vector in vacuum with ω being the angular frequency and c being the speed of light. Different from Eq. (1), the isofrequency contour of isotropic medium B is given by

$$k_x^2 + k_{Bz}^2 = \varepsilon_B k_0^2, \tag{2}$$

where k_{Bz} is the z component of the wave vector in medium B. In Eq. (1), we consider the permittivity components $\varepsilon_{Ax} > 0$ and $\varepsilon_{Az} < 0$ so that k_{Az} is a real number. In this case, the hyperbola axis of the HMM will be along the z direction.

Since only the extraordinary mode is present in the HMM layer, we can use a 2×2 transfer-matrix method [26] to study wave propagations in the 1DPCs containing HMMs, as is discussed in the Appendix. For an infinite-periodic structure $(N \to \infty)$, according to Bloch's theorem, the dispersion relation at any incident angle yields to

$$\cos(Kd) = \cos(k_{Az}d_A)\cos(k_{Bz}d_B) - \frac{1}{2}\left(\frac{\eta_{Az}}{\eta_{Bz}} + \frac{\eta_{Bz}}{\eta_{Az}}\right)\sin(k_{Az}d_A)\sin(k_{Bz}d_B), \tag{3}$$

where K is the Bloch wave vector; $\eta_{Az} = k_{Az}/(\omega\varepsilon_0\varepsilon_{Ax})$ and $\eta_{Bz} = k_{Bz}/(\omega\varepsilon_0\varepsilon_B)$ are the wave impedances in medium A and B, respectively. ε_0 is the permittivity of vacuum. Equation (3) has no real solution for K satisfying $|\cos(Kd)| > 1$, which corresponds to the gaps of 1DPCs.

The photonic gaps of 1DPCs are physically determined by Bragg reflection. At the Bragg angular frequency $\omega_{\rm Brg}$ of the first band gap, the Bragg condition is given by [5]

$$\Phi = (k_{Az}d_A + k_{Bz}d_B)|_{\omega_{\rm Brg}} = \pi, \tag{4}$$

where Φ is the total propagating phase in a unit cell of a PC. For conventional all-dielectric PCs, Eq. (2) shows that both k_{Az} and k_{Bz} will decrease as incident angle θ increases. Therefore, in order to satisfy Eq. (4), the value of $\omega_{\rm Brg}$ will increase as θ increases. This is the reason why a conventional gap is angle dependent and its dispersion has a parabolic shape. However, if we choose a HMM and a dielectric to form a 1DPC, we find the situation is quite different. Equation (1) shows that k_{Az} will increase rather than decrease with an increase of θ. This means that, with the increase of θ, Eq. (4) can be satisfied even if the value of $\omega_{\rm Brg}$ does not change. Since $\partial\Phi/\partial\theta = (\partial\Phi/\partial k_x)(\partial k_x/\partial\theta) = 0 \to \partial\Phi/\partial k_x = 0$, we differentiate Eq. (4) with respect to k_x and obtain

$$\frac{\partial\Phi}{\partial k_x} = \left(d_A\frac{\partial k_{Az}}{\partial k_x} + d_B\frac{\partial k_{Bz}}{\partial k_x}\right)\Bigg|_{\omega_{\rm Brg}} = 0. \tag{5}$$

Equation (5) must be met for all allowed k_x, which gives the condition of a dispersionless gap around $\omega_{\rm Brg}$. As is discussed above, in conventional all-dielectric PCs, $\partial k_{Az}/\partial k_x < 0$, $\partial k_{Bz}/\partial k_x < 0$ [see Fig. 2(a)], and Eq. (5) cannot be satisfied. However, HMMs exhibit anomalous dispersion of wave vectors that is different from dielectric. As is shown in Fig. 2(b), k_{Az} of HMMs will increase with

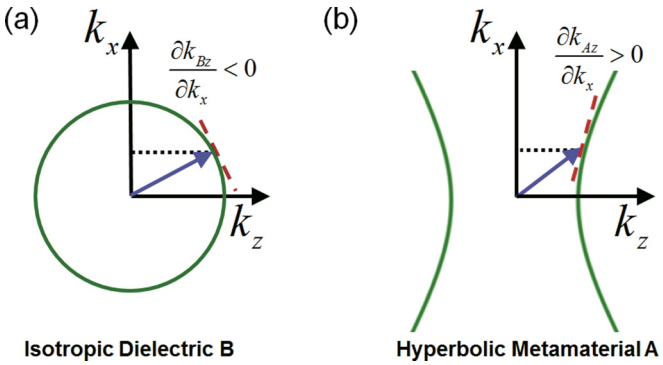

FIG. 2. (a) Dispersion of wave vector in dielectric with $\partial k_{Bz}/\partial k_x < 0$. By contrast, dispersion of wave vector in HMMs with $\partial k_{Az}/\partial k_x > 0$ is exhibited in (b).

incident angle θ, which is in contrast to the case of dielectric. The increase of k_{Az} in HMM layer A can compensate the decrease of k_{Bz} in the isotropic dielectric layer B. We call such compensation effect the *phase variation compensation effect*. Therefore, under proper parameters, a dispersionless gap around ω_{Brg} can be realized in our structure.

To obtain the parameters that satisfy phase variation compensation required by Eq. (5), we rewrite Eqs. (1) and (2) as $k_{Az} = k_0 \varepsilon_{Ax}^{1/2}[1 - k_x^2/(\varepsilon_{Az} k_0^2)]^{1/2}$ and $k_{Bz} = k_0 \varepsilon_B^{1/2}[1 - k_x^2/(\varepsilon_B k_0^2)]^{1/2}$, where $k_x \in [0, k_0]$ when light launches into a 1DPC from air. Under the conditions of $|\varepsilon_{Az}| \gg 1$ and $\varepsilon_B \gg 1$, k_{Az} and k_{Bz} can be Taylor expanded to the first-order series, i.e.,

$$k_{Az} \approx k_0 \sqrt{\varepsilon_{Ax}} \left(1 - \frac{k_x^2}{2\varepsilon_{Az} k_0^2}\right), \tag{6}$$

and

$$k_{Bz} = k_0 \sqrt{\varepsilon_B} \left(1 - \frac{k_x^2}{2\varepsilon_B k_0^2}\right). \tag{7}$$

Then we substitute the above first-order approximation of k_{Az} and k_{Bz} into Eq. (5) and obtain

$$\frac{d_B}{d_A} = \frac{\sqrt{\varepsilon_{Ax}\varepsilon_B}}{-\varepsilon_{Az}}. \tag{8}$$

Equation (8) shows that d_A and d_B rely on the permittivity of materials. Since the ratio of thicknesses must be positive definite, ε_{Az} must be negative. Then this means from Eq. (1) that the hyperbola axis must coincide with the periodic axis, in order for this dispersionless band structure to be possible. Besides, we notice that d_A and d_B are frequency dependent since HMMs are dispersive. Moreover, in the derivation of Eq. (8) we have used the first-order approximation that requires $|\varepsilon_{Az}| \gg 1$ and $\varepsilon_B \gg 1$. This means that we need to choose a suitable frequency region in which $|\varepsilon_{Az}| \gg 1$ and simultaneously select a dielectric B with high refractive index if we design dispersionless gaps based on Eq. (8). Individual values of d_A and d_B can be further deduced if we combine Eq. (8) with Eq. (4). Notice that Eq. (4) at normal incidence also can be rewritten as

$$\sqrt{\varepsilon_{Ax}} d_A + \sqrt{\varepsilon_B} d_B = \frac{\pi c}{\omega_{\mathrm{Brg}}}. \tag{9}$$

Equation (9) is usually used for designing a distributed Bragg reflector at certain frequency. Now substituting Eq. (8) into Eq. (9), we obtain

$$\begin{aligned} d_A &= \frac{\pi c}{\omega_{\mathrm{Brg}}} \frac{1}{\sqrt{\varepsilon_{Ax}}\left(1 - \frac{\varepsilon_B}{\varepsilon_{Az}}\right)}, \\ d_B &= \frac{\pi c}{\omega_{\mathrm{Brg}}} \frac{1}{\sqrt{\varepsilon_B}\left(1 - \frac{\varepsilon_{Az}}{\varepsilon_B}\right)}. \end{aligned} \tag{10}$$

Equation (10) gives analytical solutions of d_A and d_B at the designed ω_{Brg} when phase variation compensation is satisfied. Since $\varepsilon_{Az} < 0$, the thicknesses of each layer are positive definite as they should be. Based on Eq. (10), we can design 1DPCs containing HMMs to realize dispersionless gaps.

According to the effective-medium approach, the 1D metal-dielectric stack with subwavelength unit cell could be equivalent to the HMMs. A magnification of HMM layer A which possesses a substructure $(CD)_S$ is schematically shown in Fig. 1, where $(CD)_S$ is a subwavelength metal-dielectric multilayer with thickness d_C of layer C and thickness d_D of layer D. S is the number of periods of $(CD)_S$. Thus we rewrite $(AB)_N$ as $[(CD)_S B]_N$. As mentioned above, dielectric B should have a high refractive index. Therefore, dielectric B and C are selected to be Si with $n_{\mathrm{Si}} = 3.48$ (i.e., permittivity $\varepsilon_{\mathrm{Si}} = n_{\mathrm{Si}}^2 = 12.11$) [27]. Material D is selected to be indium tin oxide (ITO). ITO is a good candidate as plasmonic materials in the infrared and visible regions [28]. The plasma frequency of ITO can be engineered by controlling the doping level of Sn^{4+}. The permittivity of ITO is described by a Drude model [29,30],

$$\varepsilon_D(\omega) = \varepsilon_\infty - \frac{\omega_{pD}^2}{\omega^2 + j\omega\gamma_D}, \tag{11}$$

where ε_∞ is the high-frequency permittivity with a value of 3.9 for ITO. $\omega_{pD} = (N_0 e^2/\varepsilon_0 m^*)^{1/2}$ denotes the plasma frequency, with N_0 the free electron density, $m^* = 0.4 m_e$ the effective electron mass, and γ_D the damping frequency. Here we assume $\hbar\omega_{pD} = 2.48$ eV and set $\gamma_D = 0$ in the lossless case.

On the basis of the effective-medium approach, the components of the effective permittivity tensor in the substructure $(CD)_S$ are given by [20,21]

$$\begin{aligned} \varepsilon_{Ax} &= \varepsilon_C(1 - p) + \varepsilon_D p, \\ \varepsilon_{Az} &= \frac{1}{\frac{1-p}{\varepsilon_C} + \frac{p}{\varepsilon_D}}, \end{aligned} \tag{12}$$

where the filling ratio $p = d_D/(d_C + d_D)$ is the volume percentage of layer D in the unit cell of the substructure. We assume $d_C = d_D = 25$ nm, and thus $p = 0.5$. Optical frequencies $(\omega/2\pi)$ vary in the vicinity of 200 THz, i.e., wavelength in the vicinity of 1500 nm, which is much larger than the thickness $d_C + d_D$ of the unit cell and thus the effective-medium approach is valid. The effective permittivity tensors of the substructure $(CD)_S$ are shown in Fig. 3(a). The effective permittivity components ε_{Ax} and ε_{Az} are represented by the red and blue solid lines, respectively. $\varepsilon_{Ax} > 0$ and $\varepsilon_{Az} < 0$ in the frequency region of 150–300 THz, which corresponds to HMMs. Moreover, in the region of 150–220 THz, $|\varepsilon_{Az}| \gg 1$ and we will design ω_{Brg} in this region.

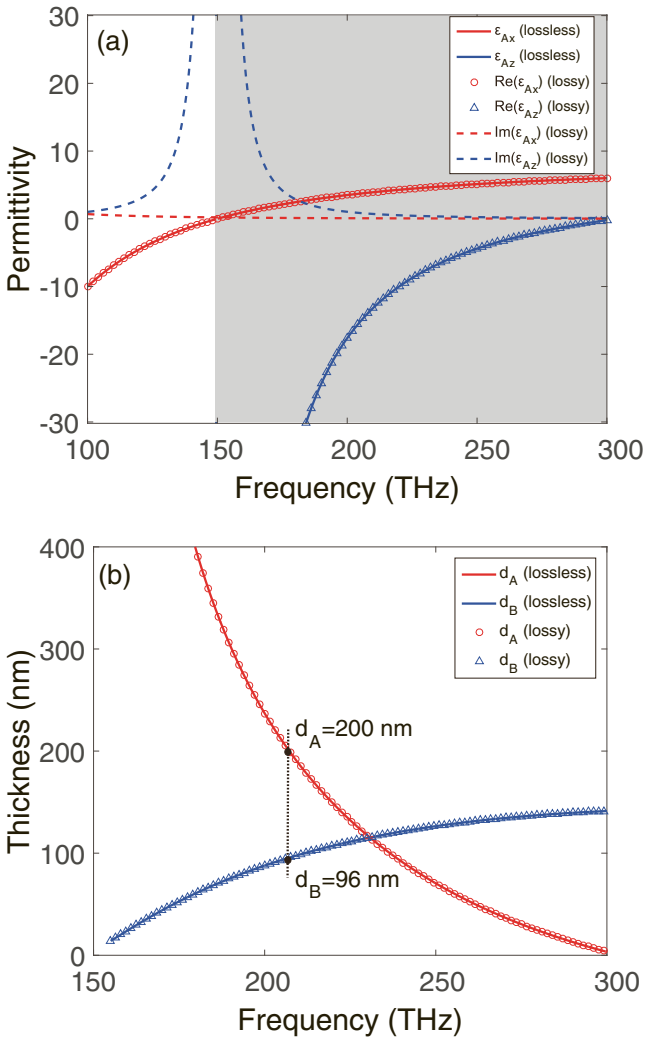

FIG. 3. (a) Effective permittivity tensor of the substructure $(CD)_S$ based on Eq. (12). $d_C = d_D = 25$ nm and $\varepsilon_C = 12.11$; ε_D is taken from Eq. (11). ε_{Ax} (ε_{Az}) is shown by the red (blue) line in the lossless case ($\gamma_D = 0$). In the lossy case ($\hbar\gamma_D = 0.016$ eV), Re(ε_{Ax}) and Re(ε_{Az}) are represented by the scattered open circles and triangles, respectively. Im(ε_{Ax}) and Im(ε_{Az}) are shown by the red and blue dashed lines, respectively. The gray region indicates the frequency region of HMMs. (b) d_A and d_B as a function of frequency based on the dispersionless condition of Eq. (10) with $\varepsilon_B = 12.11$. The solid lines correspond to the lossless case ($\gamma_D = 0$) while the scattered open circles and triangles correspond to the lossy case ($\hbar\gamma_D = 0.016$ eV).

After obtaining the permittivity of materials in the structure $(AB)_N$, we will further determine d_A and d_B. According to the dispersionless condition of Eq. (10), the frequency-dependent relation of d_A and d_B is given in Fig. 3(b). Considering that HMM layer A is composed of the substructure $(CD)_S$ with thicknesses $d_C = d_D = 25$ nm, we select $S = 4$ which corresponds to $d_A = 200$ nm. In this case the corresponding frequency is $\omega_{\mathrm{Brg}}/2\pi = 207.2$ THz and $d_B = 96$ nm, as is indicated by the dotted line in Fig. 3(b). Of course, other parameters also can be selected only if the parameters of the substructure $(CD)_S$ are proposed beforehand. Based on the above parameters, we calculate the band structure. For an infinite-periodic structure ($N \to \infty$), the dispersion relation

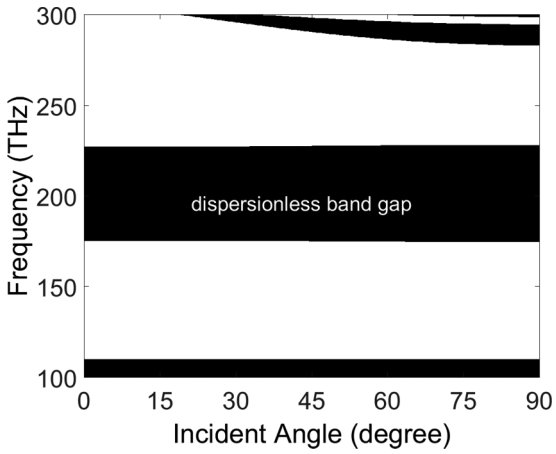

FIG. 4. Dispersion relation of an infinite-periodic structure $(AB)_N$ ($N \to \infty$) in the lossless case ($\gamma_D = 0$), where $d_A = 200$ nm, $d_B = 96$ nm, and $\varepsilon_B = 12.11$; ε_{Ax} and ε_{Az} are taken from Fig. 3(a). The black and the white areas correspond to the forbidden gaps and the allowed bands, respectively. A dispersionless gap appears in the region of 175–228 THz.

is given by Eq. (3). The photonic band gap of the structure $(AB)_N$ as a function of incident angle is illustrated in Fig. 4. It is seen that a gap indicated by the black area appears in the frequency region of 175–228 THz with the width of 53 THz. Moreover, as we expected, both the upper and the lower band edge are independent of the incident angle, owing to the phase variation compensation effect. Therefore, in the 1DPC with HMMs, we have realized a dispersionless gap with a fixed bandwidth.

We further demonstrate the dispersionless property of gaps by calculating the transmittance spectra of a finite-periodic structure. We firstly consider the $(AB)_6$ structure, where $d_A = 200$ nm, $d_B = 96$ nm, $\varepsilon_B = 12.11$, ε_{Ax}, and ε_{Az} are taken from Fig. 3(a) in the lossless case. Using the transfer-matrix method, the transmittance spectra of $(AB)_6$ at several representative angles are given in Fig. 5(a). It is seen that, for the lower band edge, the frequencies of the transmittance peak at all representative angles are 167.4 THz. For the upper band edge, the frequencies of transmittance peak at 0°, 30°, 60°, and 85° are 236.4, 236.2, 235.6, and 235.2 THz, respectively, which varies very little with incident angles. Therefore, the transmittance gap in Fig. 5(a) is an angle-insensitive gap. Then we consider the $[(CD)_4B]_6$ structure in which the substructure $(CD)_4$ mimics HMM layer A. For the effective ε_{Ax} and ε_{Az} in Fig. 3(a), ε_D is taken from Eq. (11) with $\gamma_D = 0$, $\varepsilon_C = 12.11$, and $d_C = d_D = 25$ nm. The parameters of B are unchanged. The transmittance spectra of $[(CD)_4B]_6$ at several representative angles are given in Fig. 5(b). Overall, the transmittance spectra of Fig. 5(b) are almost the same as that of Fig. 5(a) and the transmittance gap in Fig. 5(b) is also an angle-insensitive gap. Therefore, the effective-medium approach works well and the 1DPC containing the subwavelength metal-dielectric stack can be used for realizing dispersionless gaps.

For better comparison, in Fig. 6 we also show the variance of gaps with angle of incidence for conventional all-dielectric PCs in which the phase variation compensation effect is lacking.

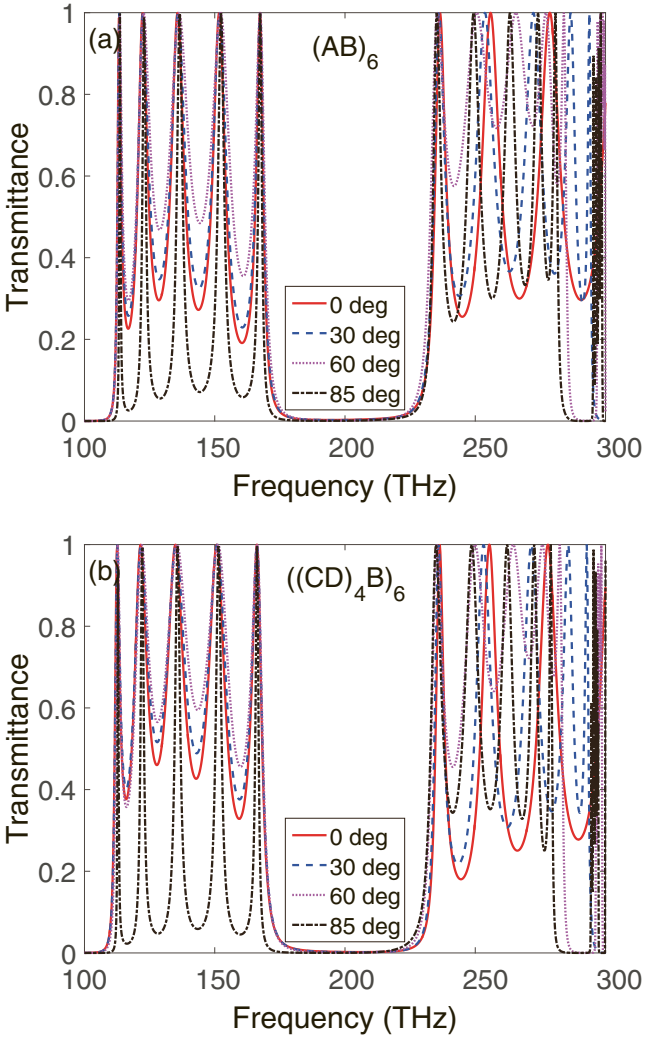

FIG. 5. (a) Transmittance spectra of a finite-periodic structure $(AB)_6$ at incident angles of 0°, 30°, 60°, and 85°, respectively. $d_A = 200$ nm, $d_B = 96$ nm, and $\varepsilon_B = 12.11$; ε_{Ax} and ε_{Az} are taken from Fig. 3(a) in the lossless case ($\gamma_D = 0$). (b) Transmittance spectra of $[(CD)_4B]_6$ at incident angles of 0°, 30°, 60°, and 85°, respectively. $d_C = d_D = 25$ nm, $d_B = 96$ nm, and $\varepsilon_B = \varepsilon_C = 12.11$; ε_D is taken from Eq. (11) with $\gamma_D = 0$.

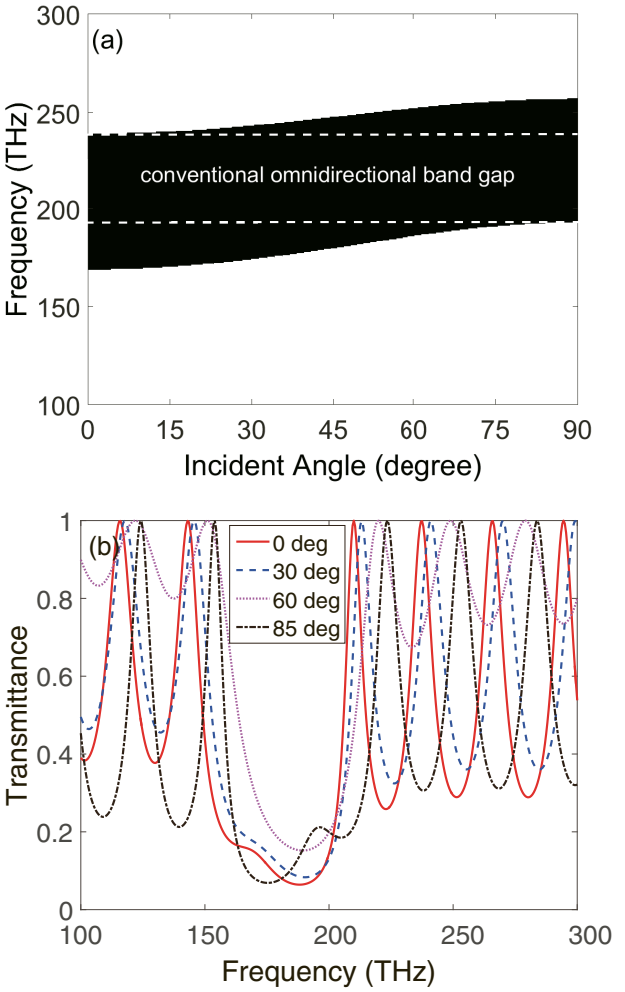

FIG. 6. (a) Band gap of a 1D SiC-Si PC with infinite periods. $\varepsilon_{SiC} = 6.6$, $\varepsilon_{Si} = 12.11$, $d_{SiC} = 200$ nm, and $d_{Si} = 96$ nm. The area between the two dotted lines indicates an omnidirectional gap. (b) Transmittance spectra of a 1D SiC-Si PC with six periods at incident angles of 0°, 30°, 60°, and 85°, respectively.

Here the conventional 1DPC is constructed by replacing the HMM layer with a SiC layer. The refractive index of SiC (denoted by n_{SiC}) is 2.57; i.e., the permittivity $\varepsilon_{SiC} = n_{SiC}^2 = 6.6$ [27]. The other parameters remain invariant. As is shown in Fig. 6(a), although an omnidirectional gap is realized from the Bragg gap in the 1D infinite-periodic SiC-Si PC, its band edges change remarkably with incident angles. In Fig. 6(b), we give the transmittance spectra of the 1D SiC-Si PC with six periods at incident angles of 0°, 30°, 60°, and 85°, respectively. Consistent with Fig. 6(a), in Fig. 6(b) the frequencies of the lower and the upper band edges both shift to the higher frequencies noticeably as the incident angle increases. Therefore, conventional all-dielectric PCs cannot possess dispersionless gaps that, by contrast, the 1DPCs with HMMs can have.

Lastly, it should be pointed out that the dispersionless gaps of 1DPCs with HMMs can be obtained only for TM polarization. In Fig. 1, if we change TM polarization to TE polarization, only an ordinary wave can be excited in the HMM layer, as is demonstrated in the Appendix. In this circumstance, the dispersion of the wave vector is similar to that of an isotropic medium. Therefore, for TE polarization, the phase variation compensation effect no longer exists and the dispersionless band gap cannot be obtained. Besides, since $\varepsilon_D(\omega)$ is dispersive, from Eq. (12) the effective ε_{Ax} and ε_{Az} may interchange their signs when frequency varies. As a result, while we change frequencies, the hyperbola axis may rotate. Therefore, a dispersionless band gap can be obtained only in the case in which the normal-incidence ω_{Brg} falls within a frequency region where the hyperbola axis is along the axis of periodicity.

B. The influence of loss

In the previous part, we investigate the phase variation compensation effect and the realization of dispersionless gaps

in the lossless case. However, γ_D is in fact a nonzero value in ITO. Therefore, it is necessary to study the impact of the loss on the phase variation compensation effect and the dispersion property of gaps. In this part, we consider the realistic value of γ_D with $\hbar\gamma_D = 0.016$ eV [29,30]. Normally, the introduction of γ_D in Eq. (11) will not only produce the imaginary part, but also change the real part of $\varepsilon_D(\omega)$. Nevertheless, in our considered frequency range, γ_D is two orders of magnitude smaller than ω. As a result, the realistic γ_D hardly changes the real part of $\varepsilon_D(\omega)$.Then, from Eq. (12), $\mathrm{Re}(\varepsilon_{Ax})$ and $\mathrm{Re}(\varepsilon_{Az})$ are nearly unchanged. To numerically confirm this point, we take $\hbar\gamma_D = 0.016$ eV and recalculate Fig. 3. In the lossy case, $\mathrm{Re}(\varepsilon_{Ax})$ and $\mathrm{Re}(\varepsilon_{Az})$ are shown by the scattered open circles and triangles, respectively, while $\mathrm{Im}(\varepsilon_{Ax})$ and $\mathrm{Im}(\varepsilon_{Az})$ are represented by the red and blue dashed lines, respectively. It is seen from Fig. 3(a) that the scattered open circles (triangles) for $\hbar\gamma_D = 0.016$ eV almost overlap with the red (blue) solid line for $\gamma_D = 0$. Accordingly, the designed thicknesses that depend on $\mathrm{Re}(\varepsilon_{Ax})$ and $\mathrm{Re}(\varepsilon_{Az})$ will also be nearly unchanged. As is shown in Fig. 3(b), the scattered open circles (triangles) for $\hbar\gamma_D = 0.016$ eV almost overlap with the red (blue) solid line for $\gamma_D = 0$. The differences of d_A or d_B between the lossless case and the lossy case are so small that we can use the structural parameters in the lossless case, i.e., $d_A = 200$ nm and $d_B = 96$ nm to study the phase variation compensation effect and the dispersion property of gaps in the lossy case.

Now we study the influence of $\mathrm{Im}(\varepsilon_{Ax})$ and $\mathrm{Im}(\varepsilon_{Az})$ on the Bragg condition. In the lossless case, k_{Az} is a real number. However, when $\mathrm{Im}(\varepsilon_{Ax})$ and $\mathrm{Im}(\varepsilon_{Az})$ of the effective HMM are considered, k_{Az} becomes a complex number. Our calculations from Fig. 3(a) show that, in the frequency region of 173–220 THz, $|\varepsilon_{Az}| \gg 1$, $\mathrm{Im}(\varepsilon_{Ax})/Re(\varepsilon_{Ax} \ll 1$, and $|\mathrm{Im}(\varepsilon_{Az})/Re(\varepsilon_{Az})| \ll 1$. In this frequency region, similar to Eq. (6), k_{Az} can be written as

$$\begin{aligned} k_{Az} &\approx k_0\sqrt{\mathrm{Re}(\varepsilon_{Ax}) + i\mathrm{Im}(\varepsilon_{Ax})} \\ &\quad\times\left\{1 - \frac{k_x^2}{2k_0^2[\mathrm{Re}(\varepsilon_{Az}) + i\mathrm{Im}(\varepsilon_{Az})]}\right\} \\ &\approx k_0\sqrt{\mathrm{Re}(\varepsilon_{Ax})}\left[1 + i\frac{\mathrm{Im}(\varepsilon_{Ax})}{2\mathrm{Re}(\varepsilon_{Ax})}\right] \\ &\quad\times\left\{1 - \frac{k_x^2}{2\mathrm{Re}(\varepsilon_{Az})k_0^2}\left[1 - i\frac{\mathrm{Im}(\varepsilon_{Az})}{\mathrm{Re}(\varepsilon_{Az})}\right]\right\}. \end{aligned} \tag{13}$$

Thus the real part of k_{Az} is given by

$$\begin{aligned} \mathrm{Re}(k_{Az}) &= k_0\sqrt{\mathrm{Re}(\varepsilon_{Ax})}\left\{1 - \frac{k_x^2}{2\mathrm{Re}(\varepsilon_{Az})k_0^2}\right. \\ &\quad\left.\times\left[1 + \frac{\mathrm{Im}(\varepsilon_{Ax})}{2\mathrm{Re}(\varepsilon_{Ax})}\frac{\mathrm{Im}(\varepsilon_{Az})}{\mathrm{Re}(\varepsilon_{Az})}\right]\right\}. \end{aligned} \tag{14}$$

Inside the parentheses of Eq. (14), the absolute value of the second term is much smaller than 1. Neglecting this term, the real part of k_{Az} can be rewritten as

$$\mathrm{Re}(k_{Az}) \approx k_0\sqrt{\mathrm{Re}(\varepsilon_{Ax})}\left[1 - \frac{k_x^2}{2\mathrm{Re}(\varepsilon_{Az})k_0^2}\right]. \tag{15}$$

Comparing Eq. (15) with Eq. (6), we find that the real part of k_{Az} in the lossy case is nearly the same as that in the lossless case for any $k_x \in [0, k_0]$. As a result, the Bragg condition hardly changes and the loss will not affect the design of dispersionless gaps based on Eq. (10) in the lossless case.

To verify the above theoretical analysis, we calculate the band structure for the real part of the Bloch wave vectors after loss is introduced. In the lossy case, the right-hand side of Eq. (3) is complex, and the dispersion relation takes the form as $\cos(Kd) = g_R + ig_I$, where $K = K_R + iK_I$ represents a complex Bloch wave vector; g_R and g_I represent the real and imaginary parts of the right-hand side of Eq. (3), respectively. After some deductions, the dispersion relation for K_R satisfies the following equation [31]:

$$\cos(K_R d) = g_R\left[\frac{g_I^2}{\sin^2(K_R d)} + 1\right]^{-1/2}. \tag{16}$$

Equation (16) is used to calculate the band structure for K_R. From Eq. (16), we see that $|\cos(K_R d)|$ cannot be equal to 1. As a result, the band edges are not as clear as those in the lossless case and the gaps with large K_I appear in the frequency regions in which $|\cos(K_R d)| \to 1$ [31,32]. Taking the values of $\mathrm{Im}(\varepsilon_{Ax})$ and $\mathrm{Im}(\varepsilon_{Az})$ in Fig. 3(a) and the other parameters used for Fig. 4, we calculate the band structure based on Eq. (16), as is shown in Fig. 7(a). Comparing Fig. 7(a) with Fig. 4 in the lossless case, we see that, although the band edges become a little bit obscure, the dispersionless property of the gaps is maintained when loss is considered.

We further illustrate the influence of loss on dispersionless property of gaps by calculating the transmittance spectra of a finite-periodic structure $[(CD)_4B]_6$, where the parameters are the same as those in Fig. 5(b) except that $\gamma_D = 0$ is changed to $\hbar\gamma_D = 0.016$ eV. The transmittance spectra at several representative angles are given in Fig. 7(b). Comparing Fig. 7(b) with Fig. 5(b), we see that the angle-insensitive property of the transmittance gap is maintained in the lossy case. Of course, because of the absorption caused by the loss, the transmittances of band edges are smaller than 1. For the upper band edge, the transmittance remains about 0.5 up to the incident angle of 85°. For the lower band edge, the transmittance remains about 0.64 when the incident angle increases to 60°, and decreases to 0.29 when the incident angle reaches 85°. Briefly, although the transmittance is reduced, the loss in the designed frequency range does not affect the dispersionless property of the gaps.

C. The dispersionless gaps with wide parameter space

The dispersionless gap mentioned above is realized according to the perfect phase variation compensation effect required by Eq. (10). In fact, our structure has a wide parameter space for the design of dispersionless gaps. If d_A and d_B that meet Eq. (10) are changed, the perfect phase variation compensation at ω_{Brg} will not be satisfied. For convenience, we only change d_B. $d_A = 200$ nm, $\varepsilon_B = 12.11$, $\mathrm{Re}(\varepsilon_{Ax})$, and $\mathrm{Re}(\varepsilon_{Az})$ are taken from Fig. 3(a). Based on Eq. (4), for each value of d_B, we plot the variance of $\omega_{\mathrm{Brg}}/2\pi$ with the incident angle, as is shown in Fig. 8(a). It is seen that $\omega_{\mathrm{Brg}}/2\pi$ is invariant with incident angle at $d_B = 96$ nm, which corresponds to the perfect phase variation compensation. Nevertheless, when the value of d_B deviates from 96 nm, i.e., the perfect phase variation compensation is not satisfied,

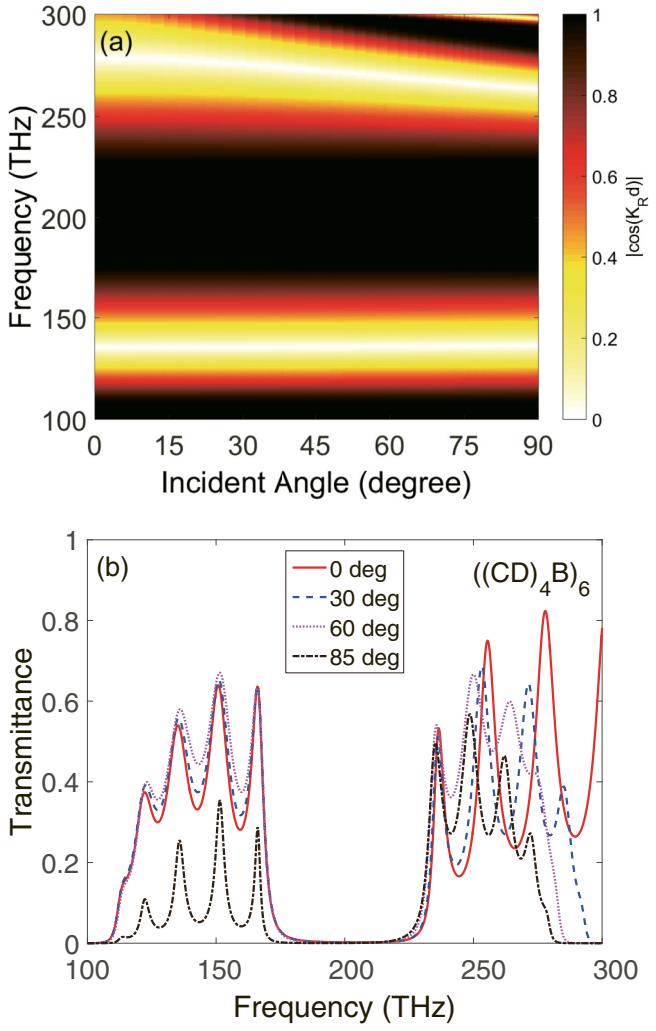

FIG. 7. (a) Dispersion relation of an infinite-periodic structure $(AB)_N$ $(N \to \infty)$ for the real part of the Bloch wave vectors in the lossy case ($\hbar\gamma_D = 0.016$ eV). The gap appears in the frequency regions in which $|\cos(K_R d)| \to 1$. $d_A = 200$ nm, $d_B = 96$ nm, and $\varepsilon_B = 12.11$; complex ε_{Ax} and ε_{Az} are taken from Fig. 3(a) in the lossy case ($\hbar\gamma_D = 0.016$ eV). (b) Transmittance spectra of $[(CD)_4B]_6$ at incident angles of 0°, 30°, 60°, and 85°, respectively. $d_C = d_D = 25$ nm, $d_B = 96$ nm, and $\varepsilon_B = \varepsilon_C = 12.11$; ε_D is taken from Eq. (11) with $\hbar\gamma_D = 0.016$ eV.

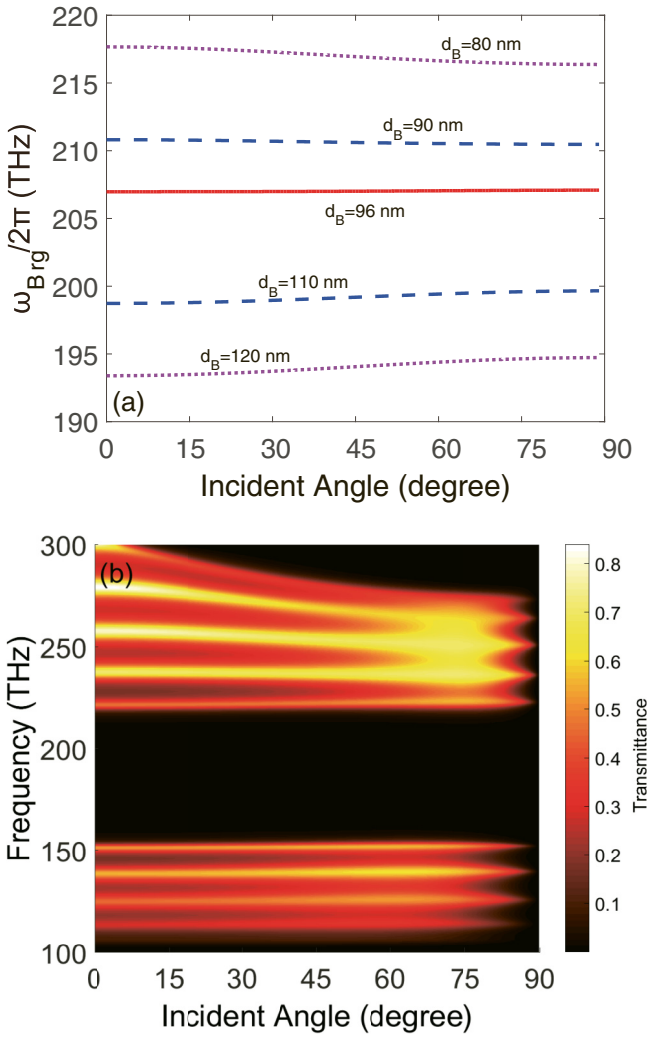

FIG. 8. (a) The dependence of $\omega_{\mathrm{Brg}}/2\pi$ on incident angle for different d_B based on Eq. (4). $d_A = 200$ nm and $\varepsilon_B = 12.11$; $\mathrm{Re}(\varepsilon_{Ax})$ and $\mathrm{Re}(\varepsilon_{Az})$ are taken from Fig. 3(a). (b) Transmittance spectrum for all angles of incidence at $d_B = 120$ nm. The other parameters are the same as those used for Fig. 7(b).

$\omega_{\mathrm{Brg}}/2\pi$ hardly changes with the incident angle. Even when the value of d_B changes to 80 or 120 nm, $\omega_{\mathrm{Brg}}/2\pi$ only slightly changes with the incident angle. Here we use a relative quantity, $\delta_{\mathrm{Brg}} = (\omega_{\mathrm{Brg},\theta} - \omega_{\mathrm{Brg},0})/\omega_{\mathrm{Brg},0}$, to denote the change of $\omega_{\mathrm{Brg}}/2\pi$ when the incident angle varies, where $\omega_{\mathrm{Brg},\theta}$ and $\omega_{\mathrm{Brg},0}$ are the ω_{Brg} at oblique incidence and at normal incidence, respectively. Our results show that the maximum of δ_{Brg} is just 0.0067 which corresponds to the case of $d_B = 120$ nm. At $d_B = 120$ nm, and the other parameters the same as those used for Fig. 7(b), we give the transmittance spectrum of the finite-periodic structure for all angles of incidence in Fig. 8(b) and still see a nearly dispersionless transmittance gap. Similar results can be obtained if we change the values of d_C, d_D, and S (i.e., d_A). Therefore, even somewhat away from the perfect phase variation compensation, the compensation effect still works well, which provides a wide parameter space to design the dispersionless gaps.

III. DISPERSIONLESS CAVITY MODES

Lastly, one important application of the dispersionless gap is to design the dispersionless cavity mode. Conventional cavity modes of planar geometry retain the angle-dependent property of gaps based on all-dielectric PCs, which can have their quality (Q) factor performance significantly reduced when not excited by a perfect plane wave. Essentially, finite-sized sources are equivalent to multiple plane waves incident at different angles. Thus, conventional 1D cavity modes will be broadened and have reduced Q factor when excited with finite-sized sources, as compared to their Q factor when excited with a plane wave [33]. By contrast, Q factors of a dispersionless cavity mode hardly change when the plane waves launch at different angles, which is very useful when the cavity mode is excited with finite-sized sources.

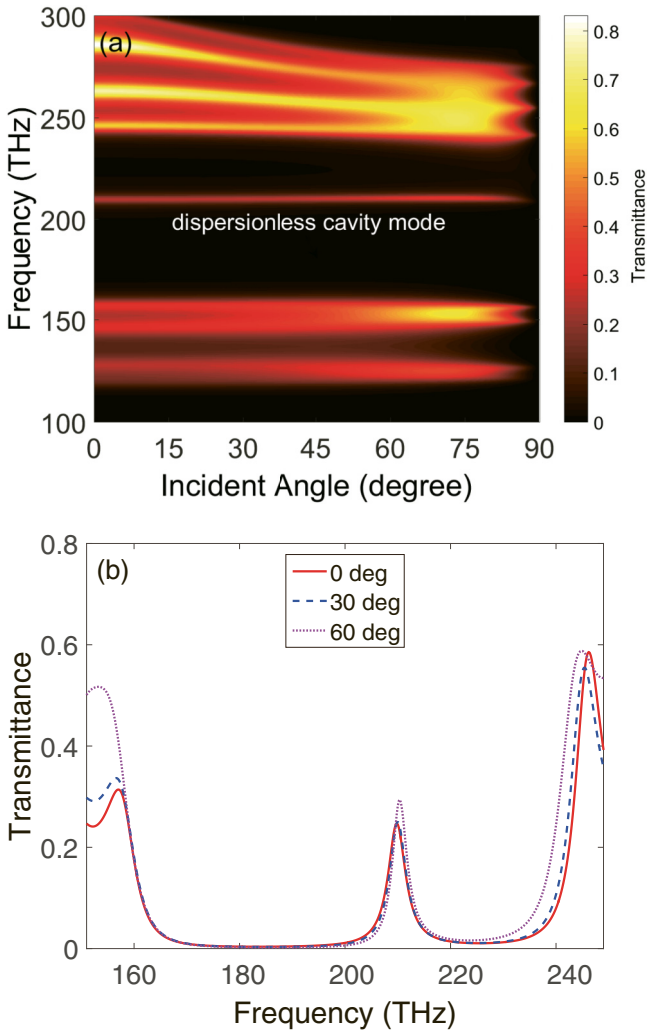

FIG. 9. (a) Transmittance spectrum of the structure $[(CD)_4B]_3B'[(CD)_4B]_3$ for all angles of incidence. $\varepsilon'_B = 12.11$, $d'_B = 100$ nm, and the other parameters are the same as those used for Fig. 7(b). A dispersionless cavity mode appears in the vicinity of 210 THz. (b) Transmittance spectra at incident angles of 0°, 30°, and 60°, respectively.

To realize dispersionless cavity modes, we insert a dielectric defect layer into the 1DPC possessing dispersionless gaps. The structure is denoted by $[(CD)_SB]_{N'}B'[(CD)_SB]_{N'}$. Here $S = 4$, $N' = 3$, and B' is selected to be Si with permittivity $\varepsilon'_B = 12.11$ and its thickness $d'_B = 100$ nm. The other parameters are the same as those used for Fig. 7(b). It is seen from Fig. 9(a) that the cavity mode inside the dispersionless gap remains nearly invariant with incident angles, owing to phase variation compensation effect. The dependence of the cavity mode on incident angle also can be quantitatively denoted with a relative quantity, $\delta_{\text{cav}} = (\omega_{\text{cav},\theta} - \omega_{\text{cav},0})/\omega_{\text{cav},0}$, where $\omega_{\text{cav},\theta}$ and $\omega_{\text{cav},0}$ are the angular frequencies of cavity modes at oblique incidence and at normal incidence, respectively. Our results show that the maximum of δ_{cav} is just 0.0029. Therefore the dependence of cavity mode on incident angle is very weak, which exhibits the dispersionless properties. To see the variance of Q factors of cavity modes, we give the transmittance spectra of the structure at three representative angles, as is shown in Fig. 9(b). It is seen that the peak positions of cavity modes at incident angles of 0°, 30°, and 60° are nearly unchanged, which is in accordance with Fig. 9(a). Besides, Q factors of cavity modes change very little at three incident angles. Of course, because of absorption, the transmittance peak values of the cavity modes are reduced from 1 in the lossless case to about 0.3. Moreover, since this nearly dispersionless cavity mode is a consequence of interference within the whole structure, its frequency position will change with the size of the defect layer. Therefore we can tune the cavity mode at the desired frequency by changing the thickness of the defect layer.

The dispersionless cavity mode obtained in our structure can be highly relevant to applications, as it enables alternative types of possible high-Q cavity modes that can be excited with quantum dot types of sources. Moreover, the dispersionless cavity modes are very beneficial in nonlinear wave mixing process. For conventional cavity modes, phase matching that is critical in coherent nonlinear optical process cannot be satisfied for all angles of incidence [34]. By contrast, the dispersionless cavity mode provides all-angle phase matching in coherent nonlinear optical process, especially in the degenerate four-wave mixing process.

IV. CONCLUSION

In summary, we reveal the phase variation compensation effect in a 1DPC composed of a HMM and a dielectric. This effect originates from the anomalous wave-vector dispersion of HMMs. Based on phase variation compensation effects, dispersionless gaps can be realized in 1DPCs containing (lossy) HMMs which are mimicked by a 1D subwavelength metal-dielectric stack. Moreover, dispersionless gaps are robust to the change of structural parameters. The simple 1D structure, together with a wide parameter space, provides a convenient method for experimental implementation of dispersionless gaps. The dispersionless gaps and cavity modes via doping the gaps will possess significant applications for all-angle reflectors, and high-Q filters excited with quantum dot types of sources as well as all-angle nonlinear wave mixing processes.

ACKNOWLEDGMENTS

This work was financially supported by the National Basic Research Program of China (Grant No. 2011CB922001), by the National Natural Science Foundation of China (Grants No. 11264003, No. 11234010, No. 11474220, No. 11404102, and No. 11504236), and by the project of Outstanding Young Teachers' Training in Higher Education Institutions of Guangxi.

APPENDIX

Generally speaking, both an extraordinary and an ordinary wave would be present in a uniaxial material such as a HMM. However, in the case where the magnetic $\boldsymbol{H}$ field of a TM polarized wave or the electric $\boldsymbol{E}$ field of a transverse-electric (TE) polarized wave is perpendicular to the optical axis of the HMM, one would obtain either only the extraordinary or only the ordinary mode. We will demonstrate this issue. We start

from the full Maxwell's equations. For the electromagnetic wave propagation in a HMM, $\boldsymbol{E}$ and $\boldsymbol{H}$ satisfy the following Maxwell equations:

$$\nabla \times \boldsymbol{E} = i\omega\mu \boldsymbol{H}, \quad \nabla \times \boldsymbol{H} = -i\omega\varepsilon_0 \bar{\bar{\varepsilon}} \cdot \boldsymbol{E}, \tag{A1}$$

where time factor $\exp(-i\omega t)$ is assumed and $\bar{\bar{\varepsilon}}$ is the relative permittivity tensor of the HMM medium. The coordinate system is selected to be the same as that shown in Fig. 1 and the HMM is assumed to have a planar geometry similar to medium A. The surface of HMM is on the xy plane and the $\bar{\bar{\varepsilon}}$ of HMM is presumed to have a diagonal form

$$\bar{\bar{\varepsilon}} = \begin{bmatrix} \varepsilon_x & & \\ & \varepsilon_x & \\ & & \varepsilon_z \end{bmatrix}, \tag{A2}$$

where ε_x and ε_z are the principle permittivity along the x (y) and z directions, respectively. From Eq. (A2), the principal axis along the z direction is the optical axis; also see Eq. (9.1-15) in Ref. [26]. Then we solve Eq. (A1) when a TM or TE plane wave propagates in the HMM with a $\bar{\bar{\varepsilon}}$ of Eq. (A2), respectively.

(1) For TM polarization, $\boldsymbol{H}$ is along the y direction which is perpendicular to the optical axis and $\boldsymbol{E}$ is on the xz plane, as is shown in Fig. 1. $\boldsymbol{E}$ and $\boldsymbol{H}$ can be written as $\boldsymbol{E} = [E_x, 0, E_z]^T \exp[i(k_x x + k_z z)]$ and $\boldsymbol{H} = [0, H_y, 0]^T \exp[i(k_x x + k_z z)]$, where E_x and E_z are the amplitudes of the x and z components of $\boldsymbol{E}$, respectively; H_y is the amplitude of the y component of $\boldsymbol{H}$; k_x and k_z are the x and z components of the wave vector, respectively. Substituting above $\boldsymbol{E}$, $\boldsymbol{H}$, and Eq. (A2) into Eq. (A1), we obtain

$$k_z H_y = \omega\varepsilon_0\varepsilon_x E_x, \tag{A3a}$$

$$k_x H_y = -\omega\varepsilon_0\varepsilon_z E_z, \tag{A3b}$$

$$k_z E_x - k_x E_z = \omega\mu_0 H_y. \tag{A3c}$$

Substituting Eqs. (A3a) and (A3b) into Eq. (A3c), we further obtain

$$\frac{k_x^2}{\varepsilon_z} + \frac{k_z^2}{\varepsilon_x} = k_0^2. \tag{A4}$$

Equation (A4) gives the dispersion of the wave vector just for an extraordinary wave. Therefore, in the case where $\boldsymbol{H}$ of a TM polarized wave is perpendicular to the optical axis of HMM, only an extraordinary wave is present.

(2) For TE polarization, $\boldsymbol{E}$ is along the y direction and $\boldsymbol{H}$ is on the xz plane. $\boldsymbol{E}$ and $\boldsymbol{H}$ can be written as $\boldsymbol{E} = [0, E_y, 0]^T \exp[i(k_x x + k_z z)]$ and $\boldsymbol{H} = [H_x, 0, H_z]^T \exp[i(k_x x + k_z z)]$, where E_y is the amplitude of the y component of $\boldsymbol{E}$; H_x and H_z are the amplitudes of the x and z components of $\boldsymbol{H}$, respectively. Substituting above $\boldsymbol{E}$, $\boldsymbol{H}$, and Eq. (A2) into Eq. (A1), we obtain

$$k_z H_x - k_x H_z = -\omega\varepsilon_0\varepsilon_x E_y, \tag{A5a}$$

$$k_z E_y = -\omega\mu_0 H_x, \tag{A5b}$$

$$k_x E_y = \omega\mu_0 H_z. \tag{A5c}$$

Substituting Eqs. (A5b) and (A5c) into Eq. (A5a), we further obtain

$$k_x^2 + k_z^2 = \varepsilon_x k_0^2. \tag{A6}$$

Equation (A6) gives the dispersion of the wave vector just for an ordinary wave. Therefore, in the case where $\boldsymbol{E}$ of a TE polarized wave is perpendicular to the optical axis of the HMM, only an ordinary wave is present.

Accordingly, in general cases a 4×4 transfer-matrix method is needed if a multilayer contains a uniaxial material because both an ordinary and an extraordinary wave would be present in the uniaxial material [35]. However, in case (1) above, a 2×2 transfer-matrix method is appropriate to solve the wave propagation in a multilayer containing a HMM because only the extraordinary wave is excited in the HMM. In the 2×2 transfer-matrix method, wave impedance for TM polarization in an anisotropic layered medium is defined by the ratio of tangential electric field and tangential magnetic field, i.e., $\eta_z = E_x/H_y = k_z/(\omega\varepsilon_0\varepsilon_x)$. Then, similar to the case in an isotropic layered medium, the dispersion relation of a 1DPC composed of a HMM and an isotropic dielectric can be derived as Eq. (3).

[1] E. Yablonovitch, Inhibited Spontaneous Emission in Solid-State Physics and Electronics, Phys. Rev. Lett. **58**, 2059 (1987).

[2] S. John, Strong Localization of Photons in Certain Disordered Dielectric Superlattices, Phys. Rev. Lett. **58**, 2486 (1987).

[3] Y. Fink, J. N. Winn, S. Fan, C. Chen, J. Michel, J. D. Joannopoulos, and E. L. Thomas, A dielectric omnidirectional reflector, Science **282**, 1679 (1998).

[4] X. Wang, X. H. Hu, Y. Z. Li, W. L. Jia, C. Xu, X. H. Liu, and J. Zi, Enlargement of omnidirectional total reflection frequency range in one-dimensional photonic crystals by using photonic heterostructures, Appl. Phys. Lett. **80**, 4291 (2002).

[5] J. Li, L. Zhou, C. T. Chan, and P. Sheng, Photonic Band Gap from a Stack of Positive and Negative Index Materials, Phys. Rev. Lett. **90**, 083901 (2003).

[6] H. T. Jiang, H. Chen, H. Q. Li, Y. W. Zhang, and S. Y. Zhu, Omnidirectional gap and defect mode of one-dimensional photonic crystals containing negative-index materials, Appl. Phys. Lett. **83**, 5386 (2003).

[7] D. Bria, B. Djafari-Rouhani, A. Akjouj, L. Dobrzynski, J. P. Vigneron, E. H. El Boudouti, and A. Nougaoui, Band structure and omnidirectional photonic band gap in lamellar structures with left-handed materials, Phys. Rev. E **69**, 066613 (2004).

[8] I. V. Shadrivov, A. A. Sukhorukov, and Y. S. Kivshar, Complete Band Gaps in One-Dimensional Left-Handed Periodic Structures, Phys. Rev. Lett. **95**, 193903 (2005).

[9] H. T. Jiang, H. Chen, H. Q. Li, Y. W. Zhang, J. Zi, and S. Y. Zhu, Properties of one-dimensional photonic crystals containing single-negative materials, Phys. Rev. E **69**, 066607 (2004).

[10] L. G. Wang, H. Chen, and S. Y. Zhu, Omnidirectional gap and defect mode of one-dimensional photonic crystals with single-negative materials, Phys. Rev. B **70**, 245102 (2004).

[11] H. T. Jiang, Y. H. Li, Z. G. Wang, Y. W. Zhang, and H. Chen, Non-Bragg band gaps and light manipulation of composite structures with metamaterials, Philos. Mag. **92**, 1317 (2012).

[12] Y. Yuan, L. X. Ran, J. T. Huangfu, H. S. Chen, L. F. Shen, and J. A. Kong, Experimental verification of zero order bandgap in a layered stack of left-handed and right-handed materials, Opt. Express **14**, 2220 (2006).

[13] L. W. Zhang, Y. W. Zhang, L. He, H. Q. Li, and H. Chen, Experimental investigation on zero-ϕ_{eff} gaps of photonic crystals containing single-negative materials, Eur. Phys. J. B **62**, 1 (2008).

[14] S. Kocaman, R. Chatterjee, N. C. Panoiu, J. F. McMillan, M. B. Yu, R. M. Osgood, D. L. Kwong, and C. W. Wong, Observation of Zeroth-Order Band Gaps in Negative-Refraction Photonic Crystal Superlattices at Near-Infrared Frequencies, Phys. Rev. Lett. **102**, 203905 (2009).

[15] S. Kocaman, M. S. Aras, P. Hsieh, J. F. McMillan, C. G. Biris, N. C. Panoiu, M. B. Yu, D. L. Kwong, A. Stein, and C. W. Wong, Zero phase delay in negative-refractive-index photonic crystal superlattices, Nat. Photonics **5**, 499 (2011).

[16] D. R. Smith and D. Schurig, Electromagnetic Wave Propagation in Media with Indefinite Permittivity and Permeability Tensors, Phys. Rev. Lett. **90**, 077405 (2003).

[17] H. N. S. Krishnamoorthy, Z. Jacob, E. Narimanov, I. Kretzschmar, and V. M. Menon, Topological transitions in metamaterials, Science **336**, 205 (2012).

[18] H. Shen, D. Lu, B. VanSaders, J. J. Kan, H. X. Xu, E. E. Fullerton, and Z. W. Liu, Anomalously Weak Scattering in Metal-Semiconductor Multilayer Hyperbolic Metamaterials, Phys. Rev. X **5**, 021021 (2015).

[19] B. Saha, G. V. Naik, S. Saber, C. Akatay, E. A. Stach, V. M. Shalaev, A. Boltasseva, and T. D. Sands, TiN/(Al,Sc)N metal/dielectric superlattices and multilayers as hyperbolic metamaterials in the visible spectral range, Phys. Rev. B **90**, 125420 (2014).

[20] A. Poddubny, I. Iorsh, P. Belov, and Y. Kivshar, Hyperbolic metamaterials, Nat. Photonics **7**, 948 (2013).

[21] L. Ferrari, C. Wu, D. Lepage, X. Zhang, and Z. W. Liu, Hyperbolic metamaterials and their applications, Prog. Quantum Electron. **40**, 1 (2015).

[22] E. E. Narimanov, Photonic Hypercrystals, Phys. Rev. X **4**, 041014 (2014).

[23] Z. Huang and E. E. Narimanov, Veselago lens by photonic hypercrystals, Appl. Phys. Lett. **105**, 031101 (2014).

[24] V. P. Drachev, V. A. Podolskiy, and A. V. Kildishev, Hyperbolic metamaterials: new physics behind a classical problem, Opt. Express **21**, 15048 (2013).

[25] S. V. Zhukovsky, A. Andryieuski, J. E. Sipe, and A. V. Lavrinenko, From surface to volume plasmons in hyperbolic metamaterials: General existence conditions for bulk high-k waves in metal-dielectric and graphene-dielectric multilayers, Phys. Rev. B **90**, 155429 (2014).

[26] P. Yeh, *Optical Waves in Layered Media* (Wiley, New York, 1988).

[27] D. Palik, *Handbook of Optical Constants of Solids I* (Academic Press, San Diego, CA, 1985).

[28] P. R. West, S. Ishii, G. V. Naik, N. K. Emani, V. M. Shalaev, and A. Boltasseva, Searching for better plasmonic materials, Laser Photonics Rev. **4**, 795 (2010).

[29] T. Gerfin and M. Grätzel, Optical properties of tin-doped indium oxide determined by spectroscopic ellipsometry, J. Appl. Phys. **79**, 1722 (1996).

[30] M. Abb, P. Albella, J. Aizpurua, and O. L. Muskens, All-optical control of a single plasmonic nanoantenna–ITO hybrid, Nano Lett. **11**, 2457 (2011).

[31] V. Kuzmiak and A. A. Maradudin, Photonic band structures of one- and two-dimensional periodic systems with metallic components in the presence of dissipation, Phys. Rev. B **55**, 7427 (1997).

[32] G. C. R. Devarapu and S. Foteinopoulou, Compact photonic-crystal superabsorbers from strongly absorbing media, J. Appl. Phys. **114**, 033504 (2013).

[33] S. Foteinopoulou and C. M. Soukoulis, Theoretical investigation of one-dimensional cavities in two-dimensional photonic crystals, IEEE J. Quantum Electron. **38**, 844 (2002).

[34] X. J. Liu, A. Rose, E. Poutrina, C. Ciracì, S. Larouche, and D. R. Smith, Surfaces, films, and multilayers for compact nonlinear plasmonics, J. Opt. Soc. Am. B **30**, 2999 (2013).

[35] P. Yeh, Electromagnetic propagation in birefringent layered media, J. Opt. Soc. Am. **69**, 742 (1979).